Electronic Supplementary Material (ESI) for Materials Chemistry Frontiers.




Supporting Information

# Zero-dimensional Cadmium-based Metal Halide with Near-Unity Photoluminescence Quantum Efficiency

Wenwen Chen,‡[a] Chuang Yang,‡[a] Shanping Wang,[a] Fang Lin,[a] Rong Chen,[a] Fengwan Guo*[ab] and Juan Wang*[a]

[a] China Ministry-of-Education Key Laboratory for the Synthesis and Application of Organic Functional Molecules
School of Chemistry and Chemical Engineering
Hubei University, Wuhan 430062 (P. R. China)

[b] Hubei Key Laboratory of Ferro & Piezoelectric Materials and Devices
Hubei University
Wuhan 430062 (P. R. China)

‡ These authors contributed equally to this work

## Experimental Procedures

***Materials***: Cadmium chloride (AR) and m-xylylenediamine were purchased from Aladdin. Antimony trichloride (99.9%) and manganese chloride (99.0%) were purchased from Macklin. Hydrochloric acid was purchased from Sinopharm Chemical Reagent Co., Ltd., and all reagents and solvents were used without further purification.

***Synthesis of $(C_8H_{14}N_2)_2CdCl_6$***: $C_8H_{12}N_2$ (1 mmol) and $CdCl_2$ (0.5 mmol) were dissolved in HCl (10 mL) at 90 ℃ and stirred for 1 hour to form a clear solution. The solution was then transferred to a programmed cooling oven, and the solution was then cooled to room temperature at a rate of 2 ℃ $h^{-1}$. The crystals were filtered and cleaned with isopropyl alcohol and dried in a furnace overnight at 30 ℃. For ion-doped $(C_8H_{14}N_2)_2CdCl_6$ crystals, a certain content of $SbCl_3$ or $MnCl_2$ is added to the hydrochloric acid system of the raw material, or $SbCl_3$ and $MnCl_2$ are added at the same time. The next operation is the same as above.

***Characterization Techniques***: Powder X-ray diffraction (PXRD) data were collected on a Rigaku D/max-IIIA diffractometer with Cu Kα (1.54 Å) radiation at 293 K. The photoluminescence excitation (PLE) and photoluminescence emission (PL) spectra were obtained on Edinburgh Instruments FLS 980. The temperature-dependent PL spectrum was measured by its matched temperature control system. The PLQY measurement and time-resolved PL (TPRL) spectra were recorded on an Edinburgh FLS 1000. The diffuse reflectance spectra of the microcrystalline powders were recorded on a UV/Vis spectrophotometer (V670-Jasco spectrophotometer) calibrated by simultaneous measurement of the substance (BaSO4 powder) and then converted to absorbance using the Kubelka-Munk theory. The actual doping concentration was measured by inductively coupled plasma atomic emission spectroscopy (ICP-AES, optimal 8000). XPS measurements were performed on Thermal Scientific Escalab 250 Xi-UPS. An Al Kα (1486.6 eV) X-ray was used as the excitation source for XPS.

***Computational Methods of the charge balance model after doping with $Sb^{3+}$***: First-principles density functional theory (DFT) is used to study the charge compensation mechanism of $Sb^{3+}$ substituted $Cd^{2+}$ in $(C_8H_{14}N_2)_2CdCl_6$. The first-principles calculations were performed using the projected augmented-wave method as implemented in the Vienna Ab initio Simulation Package (VASP). We used the VASPKIT code for post-processing of the VASP calculated data. The structural optimizations, convergence tests, and estimation of wavefunctions were adopted with the Perdew-Burke-Ernzerhof (PBE) functional. Plane-wave cutoff energy, the width of smearing and kmesh-resolved value were set to 400 eV, 0.1 eV, 0.06 Π/Å, and 20 Å, respectively. The chemical potential of Cl and H atom are calculated from the gaseous molecules within the huge lattice box. A 2*2*1 supercell containing 220 atoms was constructed to build model 1 and model 2. When estimating the formation energy, cut-off energy, and k-point mesh were set as 400 eV and the 1 × 1 × 1 Monkhorst-Pack grid, respectively. The convergence criterion for the electronic energy was $10^{-5}$ eV, whereas the structures were relaxed until the Hellmann-Feynman forces were smaller than 0.02 eV/Å.

***Computational Methods of Band structure and Density of States***: The first-principles calculations were performed using the projected augmented-wave method as implemented in the Vienna Ab initio Simulation Package (VASP). We used the VASPKIT code for postprocessing of the VASP calculated data. The structural optimizations and convergence tests were adopted with the Perdew-Burke-Ernzerhof (PBE) functional. The doped structures originate from a 2*2*2 supercell of the prototype $(C_8H_{14}N_2)_2CdCl_6$ (440 atoms) with one Cd atom replaced by the Sb atom, which corresponds to 12.5% doping content. The plane-wave cut off energy, the width of smearing, and kmesh-resolved value were set to 500 eV, 0.05 eV, and 0.03 2π/Å, respectively. The convergence criterion of the total energy was $10^{-5}$ eV/atom, and the residual Hellmann-Feynman force was 0.02 eV/Å. The GGA+U methods were applied to calculate the band structure and density of states. Within the GGA+U scheme, a single effective parameter, Ueff = U - J, is used for Mn and Sb, respectively.

Table S1. ICP-AES data of X% $Sb^{3+}$-doping $(C_8H_{14}N_2)_2CdCl_6$ SCs

| $(C_8H_{14}N_2)_2CdCl_6$: X% Sb | Sb(mg/L) | Cd(mg/L) | Ratio(Sb/Cd) |
|---|---|---|---|
| X=10 | 0.027 | 8.692 | 0.29% |
| X=20 | 0.043 | 6.162 | 0.64% |
| X=30 | 0.077 | 8.341 | 0.85% |
| X=40 | 0.155 | 10.740 | 1.33% |

Table S2. DFT simulation of two different charge balance forms after doping with $Sb^{3+}$.

| | $E_p$(eV) | $E_d$(eV) | $\mu_{Sb}$(eV) | $\mu_{Cd}$(eV) | $\mu_H$(eV) | $\mu_{Cl}$(eV) | $E_f$(eV) |
|---|---|---|---|---|---|---|---|
| Case 1 | -1214.86 | -1219.59 | -3.86 | -0.73 | | -1.78 | 9.63 |
| Case 2 | -1210.81 | -1219.59 | -3.86 | -0.73 | -0.03 | | 11.94 |

Where $E_f$ is the formation energy; $E_d$ and $E_p$ are the total energies of the doped and undoped crystals, respectively; $\mu_{Sb}$ and $\mu_{Cl}$ are the chemical potentials of the added Sb and Cl atoms, respectively; $\mu_{Cd}$ is the chemical potential of the removed Cd atom.

Table S3. ICP-AES data of X% $Mn^{2+}$-doped $(C_8H_{14}N_2)_2CdCl_6$ SCs

| $(C_8H_{14}N_2)_2CdCl_6$: X% Mn | Mn(mg/L) | Cd(mg/L) | Ratio(Mn/Cd) |
|---|---|---|---|
| X=5 | 0.012 | 11.300 | 0.22% |
| X=20 | 0.040 | 10.990 | 0.74% |
| X=30 | 0.147 | 21.040 | 1.43% |
| X=40 | 0.171 | 14.630 | 2.39% |

Table S4. ICP-AES data of $X_1$% $Sb^{3+}$-doped and $X_2$% $Mn^{2+}$-doped $(C_8H_{14}N_2)_2CdCl_6$ SCs

| $(C_8H_{14}N_2)_2CdCl_6$: $X_1$% Sb and $X_2$% Mn | Sb(mg/L) or Mn(mg/L) | Cd(mg/L) | Ratio(Sb/Cd or Mn/Cd) |
|---|---|---|---|
| $X_1$=30 | 0.092 | 21.375 | 0.40% |
| $X_2$=70 | 0.249 | 21.375 | 2.38% |

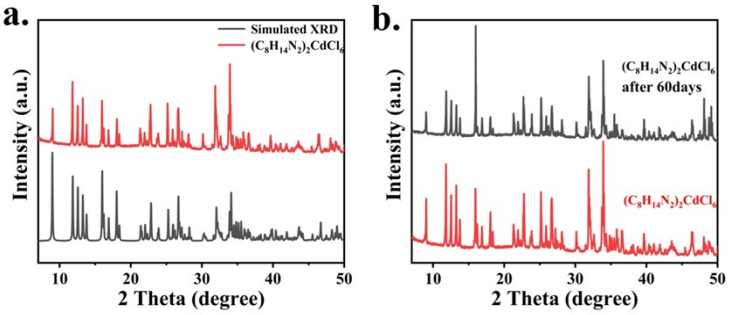


**Figure S1.** (a) PXRD patterns of $(C_8H_{14}N_2)_2CdCl_6$ SCs and simulated PXRD of $(C_8H_{14}N_2)_2CdCl_6$ SCs. (b) PXRD patterns of $(C_8H_{14}N_2)_2CdCl_6$ SCs before and after storage at room temperature for 60 days.

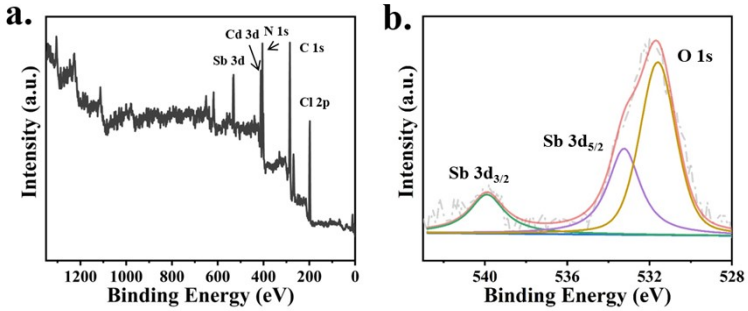


**Figure S2.** (a) XPS spectrum of $(C_8H_{14}N_2)_2CdCl_6$: $Sb^{3+}$. (b) XPS analysis of Sb 3d in $(C_8H_{14}N_2)_2CdCl_6$: $Sb^{3+}$.

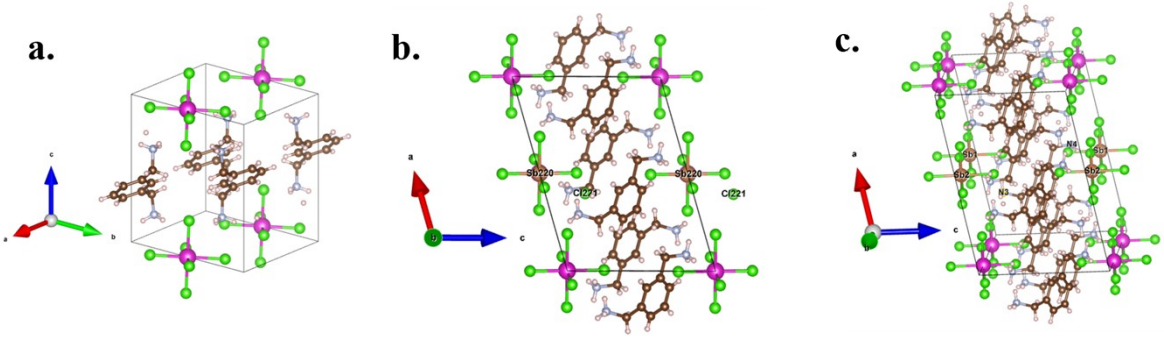


**Figure S3.** (a) The optimized structure of $(C_8H_{14}N_2)_2CdCl_6$. (b) Model A, one $Sb^{3+}$ occupies the one lattice site of $Cd^{2+}$, generating one interstitial $Cl^-$ ion in the lattice. (c) Model B, two $Sb^{3+}$ substituting two $Cd^{2+}$, making one $C_8H_{12}N_2$ replace one $C_8H_{14}N_2^{2+}$ ion.

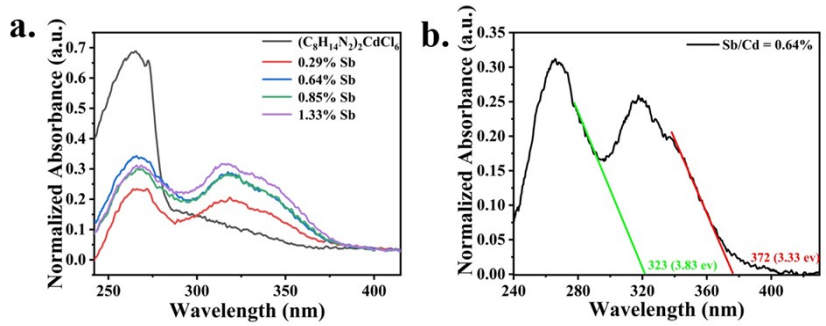


**Figure S4.** (a) Optical absorption spectra of $(C_8H_{14}N_2)_2CdCl_6$ and $(C_8H_{14}N_2)_2CdCl_6$: $Sb^{3+}$. (b) Absorption band edge fitting of 0.64% $Sb^{3+}$-doped $(C_8H_{14}N_2)_2CdCl_6$.

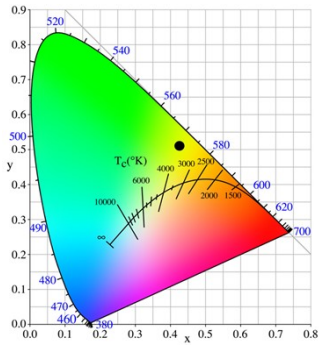


**Figure S5.** CIE chromaticity coordinate of $(C_8H_{14}N_2)_2CdCl_6$: 0.64% $Sb^{3+}$.

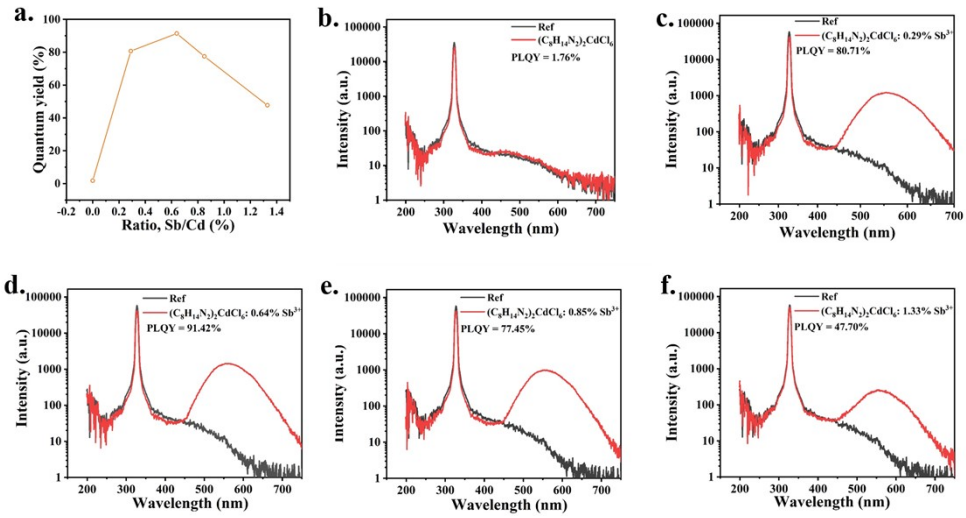


**Figure S6.** The PLQY of $Sb^{3+}$-doped $(C_8H_{14}N_2)_2CdCl_6$ with different $Sb^{3+}$ contents.

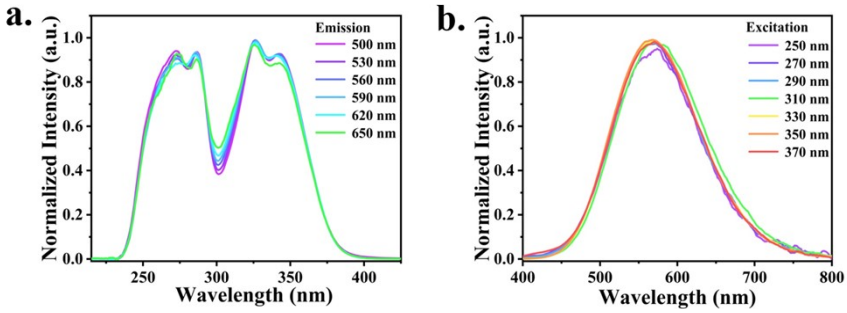


**Figure S7.** (a) The emission spectrum under different excitation wavelengths (from 250 nm to 370 nm with an interval of 20 nm) and (b) excitation spectrum under different excitation wavelengths (from 500 nm to 650 nm with an interval of 30 nm) of $(C_8H_{14}N_2)_2CdCl_6$: 0.64% $Sb^{3+}$.

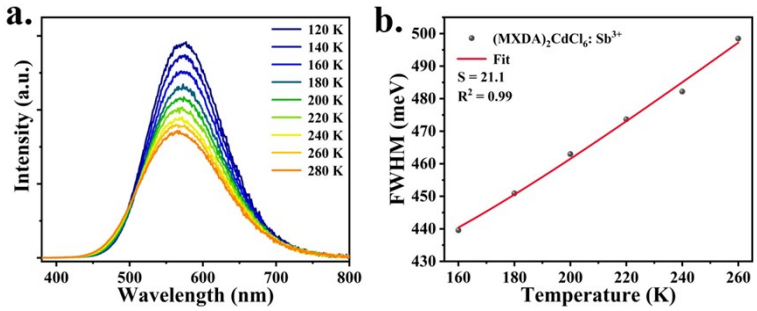


**Figure S8.** (a) Temperature-dependent PL spectrum of $Sb^{3+}$-doped $(C_8H_{14}N_2)_2CdCl_6$ under 327 nm excitation. (b) FWHM of the PL spectrum as a function of temperature for $(C_8H_{14}N_2)_2CdCl_6$: 0.64% $Sb^{3+}$ and the red line is the fitted curve.

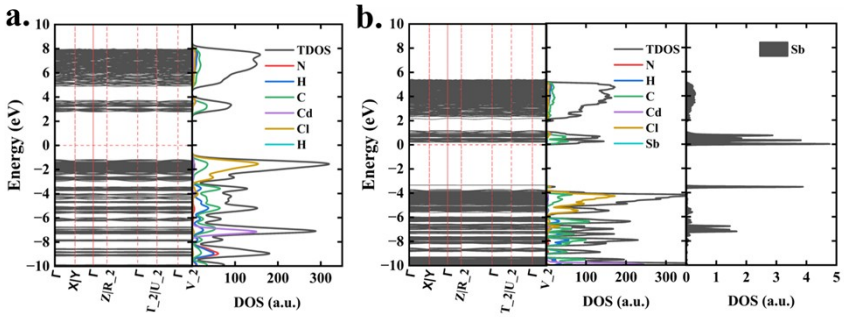


**Figure S9.** (a) Density of states of $(C_8H_{14}N_2)_2CdCl_6$ and (b) $Sb^{3+}$-doped $(C_8H_{14}N_2)_2CdCl_6$.

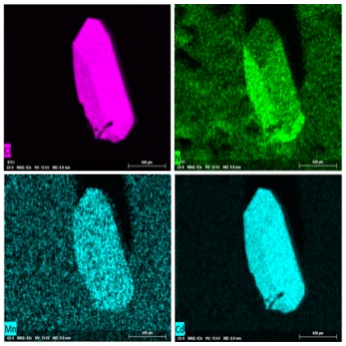

**Figure S10.** EDS mapping of the 1.43% $Mn^{2+}$-doped $(C_8H_{14}N_2)_2CdCl_6$ sample.

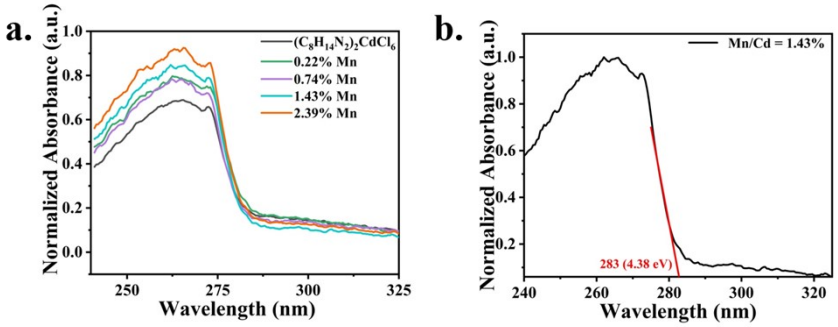


**Figure S11.** (a) Optical absorption spectra of $(C_8H_{14}N_2)_2CdCl_6$ and $(C_8H_{14}N_2)_2CdCl_6$: $Mn^{2+}$. (b) Absorption band edge fitting of 1.43% $Mn^{2+}$-doped $(C_8H_{14}N_2)_2CdCl_6$.

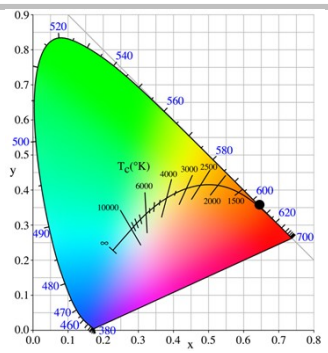


**Figure S12.** CIE chromaticity coordinates of $(C_8H_{14}N_2)_2CdCl_6$: 1.43%$Mn^{2+}$.

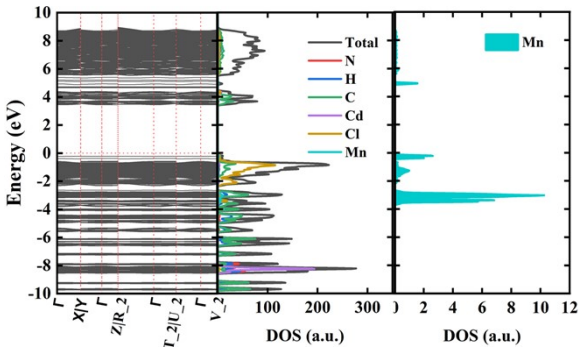


**Figure S13.** (a) The density of states of $Mn^{2+}$-doped $(C_8H_{14}N_2)_2CdCl_6$.

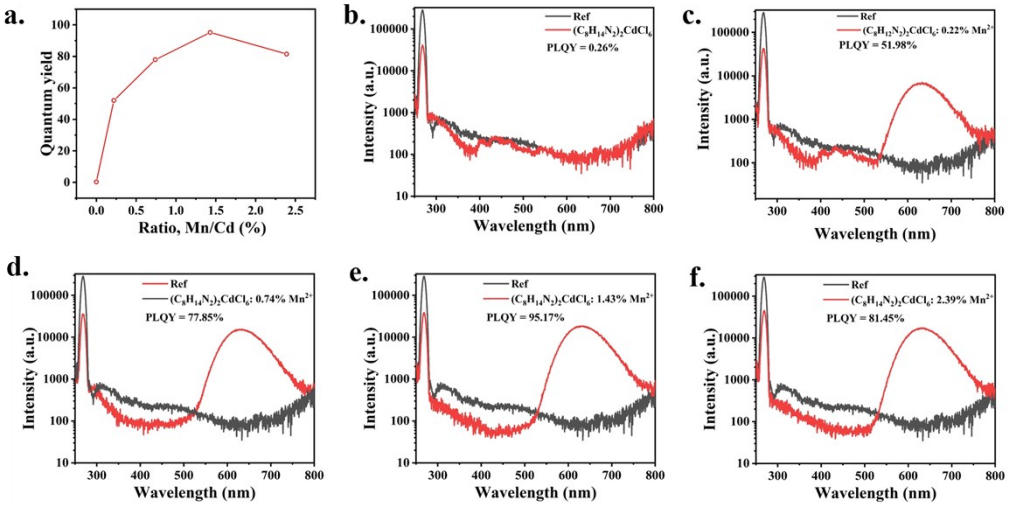


**Figure S14.** The PLQY of $Mn^{2+}$-doped $(C_8H_{14}N_2)_2CdCl_6$ with different $Mn^{2+}$ contents.

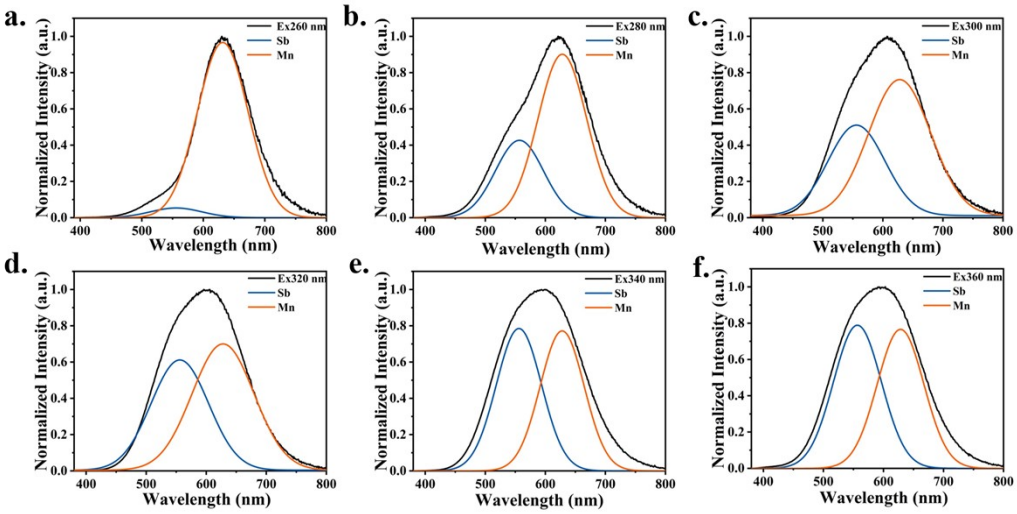


**Figure S15.** Contribution of PL intensity for Sb and Mn luminescence centers.